Journal of Materials Processing Tech. 328 (2024) 118420

Contents lists available at ScienceDirect

Journal of Materials Processing Tech.

journal homepage: www.elsevier.com/locate/jmatprotec

Conformal polishing of a glass microlens array through oxyhydrogen flame-induced viscoelasticity flow at nano/microscale

Jin Tang [a], Yi Zhang [b], Xingzhan Li [b], Qian Wang [b], Peng Zhou [b], Linfeng Zhang [a], Quanpeng He [a,*], Hui Deng [a,c,**]

[a] Department of Mechanical and Energy Engineering, Southern University of Science and Technology, Shenzhen, Guangdong 518055, China
[b] Huawei Technologies Co., Ltd., Shenzhen, Guangdong 518129, China
[c] Shenzhen Engineering Research Center for Semiconductor-specific Equipment, Department of Mechanical and Energy Engineering, Southern University of Science and Technology, Guangdong, Shenzhen 518055, China

ARTICLE INFO

Keywords:
Polishing
Ultrasmooth surface
Oxyhydrogen flame
Microlens
Viscoelasticity flow

ABSTRACT

Glass microlens arrays with small unit sizes and high integration capacities are widely utilized in various optical systems, but the femtosecond laser milling produces microscale residual steps and nanoscale rough topography on microlens surface. Accordingly, an oxyhydrogen flame polishing is proposed after femtosecond laser milling, aiming to efficiently fabricate the ultrasmooth surface without damaging shape accuracy by triggering a viscoelasticity flow at nano/microscale. Through simultaneous modelling of the polishing process, a large thermal power results in a high viscoelasticity flow velocity for nanoscale topography smoothing, followed by microscale step melting. Then, a single-point polishing experiment is conducted to determine the critical transition temperatures for nanoscale smoothing and microscale melting. It is further experimentally applied to achieve an ultrasmooth surface of cylindrical microlens array with its roughness less than 0.2 nm and no hydroxyl introduction. This process also effectively repairs subsurface damage and reduces the form error to ±0.5 μm, improving the surface quality and shape accuracy. Similar results are also observed for the polishing of spherical microlenses. In conclusion, the method of combining femtosecond laser milling and oxyhydrogen flame polishing holds promise for high-efficiency and high-quality fabrication of glass components with micro features.

1. Introduction

A glass microlens array with a small unit size ranging from the millimetre scale to the nanometre scale and high integration allows for many superior functions over traditional optical components. Glass microlens arrays have been widely used in the field of 3D imaging because of their high integration and ability to acquire more 3D images (Brar et al., 2010). Wang et al. (2015) used a microlens array for beam shaping, and the principles were comprehensively analyzed. Liang et al. (2022) used a microlens array fabricated from diamond for wavefront detection, and the relative measurement error was calculated to be 7.4%. In the early stages, reactive ion etching (RIE) combined with photolithography was the most widely used technique for manufacturing glass microlens arrays with high surface quality and good form accuracy; however, as discussed by Savander (1994), the efficiency of these methods is too low for industrial applications. Hereto, micro-silicon needle inkjet printing was proposed by Bardinal et al. (2007) to fabricate an ultrasmooth photoresist microlens array with an efficiency of 0.2–60 s per piece; however, the form accuracy fluctuated due to the uncertain interaction between the droplet and glass substrate. To overcome the problem of low manufacturing efficiency, Sohn et al. (2019) used femtosecond laser milling combined with CO_2 laser polishing to fabricate a microlens array in silica glass for beam shaping. Alternatively, Du et al. (2022) utilized single-point diamond turning to produce high-precision microstructure moulds on a nickel alloy substrate. Zhang et al. (2022) used moulding to press a microlens array on glass. These subtractive manufacturing methods can be used to efficiently fabricate glass microlens arrays with stable form accuracy; however, the thermal energy and mechanical force inevitably introduce surface/subsurface damage, which leads to poor optical performance. Currently, high-efficiency and high-quality fabrication of glass microlens arrays

* Corresponding author.
** Corresponding author at: Department of Mechanical and Energy Engineering, Southern University of Science and Technology, Shenzhen, Guangdong 518055, China.
E-mail addresses: heqp@sustech.edu.cn (Q. He), dengh@sustech.edu.cn (H. Deng).

https://doi.org/10.1016/j.jmatprotec.2024.118420
Received 29 January 2024; Received in revised form 16 April 2024; Accepted 22 April 2024
Available online 27 April 2024

Nomenclature

C_p	specific heat at constant pressure (J/(kg·K))	ρ	glass density (kg/m^3)
d_s	working distance (mm)	D	nozzle diameter (mm)
ef	form error (μm)	d_w	thermal transmission depth (mm)
g	gravity acceleration (m/s^2)	e_v	profile variation (μm)
h_{m0}	initial height (mm)	h_m	microlens height (mm)
P	thermal power (W)	k	thermal conductivity (W/(m·K))
Q	gas flow (slm)	p	atmosphere pressure (Pa)
q	heat flux vector (W/m^2)	Q_s	heat source (W/m^3)
r_s	curvature radius (mm)	R	molar gas constant (8.31 J/(mol·K))
T_h	preheating temperature (°C)	Sa	surface roughness (nm)
T_w	transient temperature (°C)	T_m	transition temperature (°C)
v_f	viscoelasticity flow with a velocity (mm/s)	t_s	simulation time (s)
$\mathbf{f}_{\mathrm{rm}}$	relaxation function of stress	v_s	scanning velocity (mm/s)
$\mathbf{K}$	viscous stress tensor (Pa)	$\mathbf{I}$	identity matrix
$\mathbf{S}$	strain-rate tensor	$\mathbf{n}$	normal vector
$\mathbf{u}$	velocity field	$\mathbf{T}_e$	viscoelastic stress tensor (N/m^2)
σ	Stefan-Boltzmann constant (5.67×10^{-8} W/(m^2·K^4))	ε	material surface emissivity
		σ_s	tension coefficient
		μ_{em}	Polymer viscosity (Pa·s)

has not been realized.

To improve the surface quality of microlens arrays, several researchers have focused on postprocessing technologies after geometrical shape fabrication. Huang et al. (2018) utilized thermal reflow polishing to fabricate microlens arrays in photoresists, and the surface roughness was reduced to 15 nm, which improved the surface quality during subsequent reactive ion etching. Through maskless fluid jet polishing, Wang et al. (2022) fabricated a 25-nm-thick *Ra* microlens array surface on a nickel alloy substrate, which was further used for glass moulding. Hydrofluoric acid etching was also employed by Feng et al. (2010) to decrease the surface roughness of spherical microlens arrays fabricated by femtosecond laser-dotting. In addition, Zhang and Yan (2022) coated a nanoscale-thick amorphous carbon layer on the microlens surface of a silicon wafer by atmospheric pressure chemical vapour deposition, which drastically decreased the surface roughness to 1 nm or less. The polishing of silica glass has been the subject of extensive research. Weingarten et al. (2017) employed a CO_2 laser for the rapid polishing of silica glass, achieving significant results with a working time of only 7 seconds for each point. In addition, researchers have also tried polishing moulded materials. Pfefferkorn et al. (2013) performed pulsed laser polishing on a Ti6Al4V mould with a velocity of 2.3 mm^2/s. Although nanometre surface roughness could be achieved by these methods, maintaining the microlens form accuracy was difficult owing to the localized thermal effect of laser melting. Furthermore, the temperature during laser polishing is affected by the distance from the focal point to the sample surface. When polishing a microlens array, Du et al. (2023) reported that different height positions of the microstructure induce different temperatures, resulting in uneven polishing. In fact, microlens formation and polishing could be synchronously achieved at 1–3 s by inducing a thermal-gradient viscoelasticity flow in hot embossing, as reported by Cheng (2021), on the polymer substrate. However, whether viscoelastic flow can be applied to silica glass, which has a much greater softening point, has not been determined.

In contrast to intermittent laser thermal transmission, oxyhydrogen flame transmission was first reported by Wang and Zupko (2006) to produce a continuous combustion thermal field with high stability, and premixed gas might increase the thermal transmission rate against post-mixed gas (Mahrenholtz, 2008). Changming et al. (2013) used fused silica powder for high-purity glass column production. Ma et al. (2021)also proposed fibre melting and shaping with an oxyhydrogen flame to enhance the interaction with the external state in refractometer manufacturing. Through thermal energy adjustment, Zhao et al. (2020) improved the use of an oxyhydrogen flame to weld a Fabry—Perot cavity probe encased in a silica capillary with high accuracy and reliability. In addition, Qiao et al. (2010) explored oxyhydrogen flame polishing of millimetre-sized optical structures, and the fabricated microlens exhibited good imaging performance at 5× magnification. Nevertheless, owing to the limited control over the oxyhydrogen flame temperature and beam spot size, the surface roughness after polishing still does not reach less than 1 nm. In a study by Ross et al. (2020), an oxyhydrogen flame at approximately 1850 °C was employed to polish silica glass following laser-assisted etching, resulting in a reduction in its roughness *Ra* from 48.7 nm to 2.26 nm.

For the process mechanism of energy beam polishing, a simulation technique is generally used to model the material flow process, wherein the initial parameter setting mainly depends on experimental data, as reported by Matthews et al. (2015). To predict the flow of materials, the thermal simulation model was first applied to laser polishing by Hildebrand et al. (2011). Through computational fluid dynamics analysis, Marimuthu et al. (2015) extracted the input thermal energy as a key factor in the molten pool convection of TC4. Since the thermal generation of oxyhydrogen flames differs from that of lasers, it is necessary to calculate the combustion thermal field derived from oxyhydrogen flames. Based on combustion thermal analysis at different gas ratios, Yao et al. (2015) further revealed the outstanding influence of thermal energy on droplet diameter in the flame hydrolysis deposition of silica glass. To improve the practicality of the simulation, Zhang et al. (2024) coupled viscoelastic fluid and airflow in the simulation and provided multiscale explanations for the polishing process of β-Ga_2O_3. However, these simulations have not yet modelled viscoelastic flow at the nanoscale or microscale of microlens arrays, and the prediction of post-polishing profiles is still difficult.

In this study, choosing the efficient and versatile femtosecond laser enables the milling of various complex shapes of microlens on silica glass. However, the residual steps and rough surface topography generated by the femtosecond laser milling may seriously affect microlens imaging quality, which should be eliminated to reach the surface roughness of less than 5 nm for industrial applications (Yuan et al., 2019; Microlens Array Specifications by Coherent Corp) Accordingly, the oxyhydrogen flame polishing of microlenses was proposed after the femtosecond laser milling. In the polishing process, nano-to-micro viscoelasticity flow on the microlens surface is triggered by precisely regulating the transient temperature. The objective is to realize the high-efficiency fabrication of ultrasmooth microlens surfaces with no shape accuracy damage. First, the microlens smoothing process, including nanoscale topography smoothing and microscale step melting,

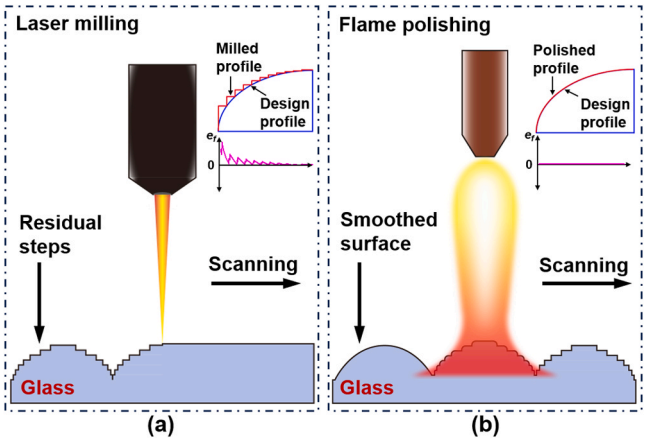

Fig. 1. Fabrication process of glass microlens arrays. (a) Femtosecond laser milling. (b) Oxyhydrogen flame polishing.

is simulatively modelled with viscoelasticity flow. Through single-point polishing, the influence of the transient temperature on the smoothing effect is investigated to determine the threshold for nano/micro-scale smoothing. Finally, oxyhydrogen flame polishing of cylindrical microlens arrays and spherical microlens at suitable transient temperatures is conducted to investigate the surface topography, roughness, form error and subsurface damage (SSD).

2. Nano/micro viscoelasticity flow smoothing of microlenses

2.1. Scheme of microlens array fabrication

Femtosecond laser milling is a precise microfabrication technique employed to create microlens arrays on silica glass substrates (Kostyuk et al., 2016). During laser milling, the designed profile of microlens is converted into a laser milling path. Except for rough topography caused by molten chip, the microlens surface will produce residual steps according to the laser diffraction limit, as shown in Fig. 1a. The deviation between laser milling profile (red line) and design profile (blue line) in the upper right corner of the microlens profile is defined as form error e_f. Herein, the residual steps are the main source of e_f. To solve the above-mentioned problems, an oxyhydrogen flame polishing is applied as a post-treatment method. After the microlens was heated during polishing, the steps gradually melted to decrease the deviation, and finally forming a smooth surface with its profile approaching to the design one, as shown in Fig. 1b.

Fig. 2 shows the scheme of oxyhydrogen flame polishing for ultrasmooth microlens surface fabrication. The oxyhydrogen flame with gas flow Q is squeezed from the copper nozzle and moves along the silica glass at scanning velocity v_s and working distance d_s. Accordingly, the large amount of thermal energy transferred from the oxyhydrogen flame to the microlens surface produces a high transient temperature T_w, and its thermal transmission depth d_w may cover the whole microlens height h_m. When T_w reaches the glass transition temperature T_m or even higher, viscoelasticity flow with a velocity v_f is triggered to smooth the microlens surface under tension and gravity. The residual steps are completely melted and rapidly flow at the microscale. By filling the high points with the low points, conformal polishing is achieved, resulting in a microlens form error e_f of less than 1 μm. Moreover, the rough nanoscale topography is smoothed to form a plane with atomic-scale roughness and less SSD. As a result, an ultrasmooth microlens surface may be efficiently achieved without damaging the shape accuracy by nano-to-micro viscoelasticity flow smoothing.

2.2. Simulative modelling of nano-to-micro viscoelasticity flow smoothing

The thermal transfer module and polymer fluid module of COMSOL Multiphysics 6.1 are used to simulate the nano-to-micro smoothing process with viscoelasticity flow on the microlens surface, as shown in Fig. 2. First, the thermal transfer process from oxyhydrogen flame to microlens is modelled to investigate the microlens temperature sensitivity. The thermal energy input into the microlens is calculated by Eqs.

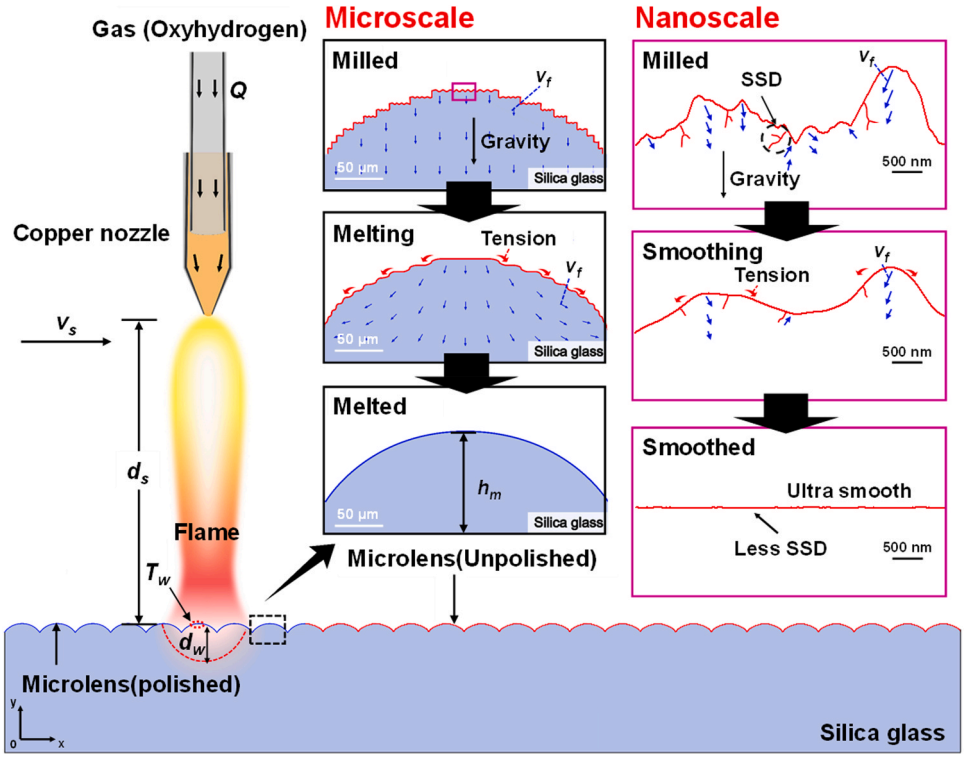

Fig. 2. Scheme of oxyhydrogen flame polishing for ultrasmooth microlens surface fabrication.

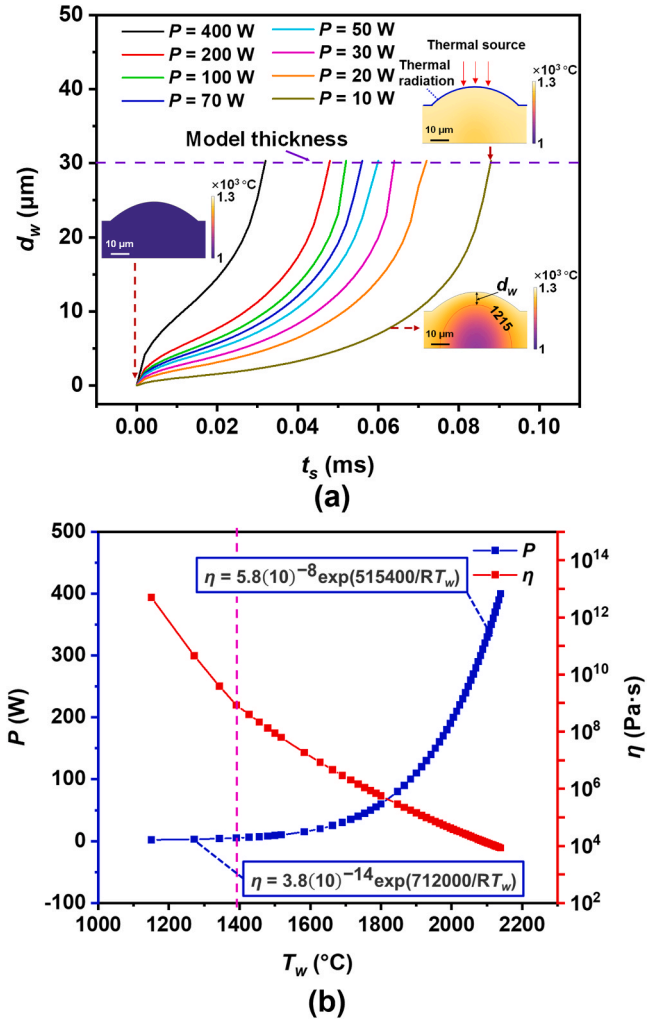

Fig. 3. Thermal transfer process of microlens. (a) Thermal transmission depth d_w of single microlens at a thermal power P of 10–400 W. (b) Correlations between fluid viscosity η, thermal power P and transient temperature T_w.

(1) and (2), and the radiation losses from the microlens surface is calculated by Eq. (3). They are described as follows:

$$\rho Cp\frac{\partial T}{\partial t}+\rho Cp\mathbf{u}\cdot\nabla Tw+\nabla\cdot\boldsymbol{q} = Qs \tag{1}$$

$$\boldsymbol{q} = -k\nabla Tw \tag{2}$$

$$-\mathbf{n}\cdot\boldsymbol{q} = -\varepsilon\sigma(T_{amb}^{4}-T_{w}^{4}) \tag{3}$$

where ρ is the density of silica glass (2203 kg/m^3), C_p is the specific thermal at constant pressure (703 J/(kg·K)), k is the thermal conductivity of silica glass (1.38 W/(m·K)) (Corning Fused SilicaTechnical Data Sheet), $\mathbf{u}$ is the velocity field (m/s), Q_s is the thermal source of oxyhydrogen flame (W/m^3), T_w is the instantaneous temperature of silica glass (°C), $\boldsymbol{q}$ is the thermal flux vector (W/m^2), $\mathbf{n}$ is the normal vector, ε is the material surface emissivity (0.86), and the σ is the Stefan-Boltzmann constant (5.67×10^{-8} W/(m^2·K^4)).

Based on the temperature sensitivity verification by the thermal transfer model, the polymer fluid model could be developed. In this model, the viscoelasticity flow is assumed to be an incompressible isothermal flow, which is also driven by tension and gravity. The tension only acts on the free surface of the microlens, and its direction is tangent to the surface profile. Thus, the corresponding momentum equation is described as follows:

$$\mathbf{n}\cdot[-p\mathbf{I}+\mathbf{K}+\mathbf{T}e] = \sigma_s(\nabla\mathrm{t}\cdot\mathbf{n})\mathbf{n}-\nabla t\sigma_s \tag{4}$$

$$\mathrm{T}_e = \sum_{\mathrm{m}}\mathrm{T}_{em} \tag{5}$$

where p is the atmospheric pressure (1.01×10^5 Pa), $\mathbf{I}$ is the identity matrix (unitless), $\mathbf{K}$ is the viscous stress tensor (Pa), $\mathbf{T}_e$ is the viscoelastic stress tensor (N/m^2) and σ_s is the tension coefficient (0.342) (Boyd et al., 2012; He et al., 2018). Due to the viscoelasticity flow with complex rheological behaviour, $\mathbf{T}_e$ is defined as the sum of the individual modes.

Gravity acts on the whole microlens, and its direction is always perpendicular to the y-axis. Thus, the corresponding momentum equation is described as follows:

$$\rho\frac{\partial\mathbf{u}}{\partial t}+\rho(\mathrm{u}\cdot\nabla)\mathbf{u} = \nabla\cdot[-p\mathbf{I}+\mathbf{K}+\mathbf{T}e]+\rho g \tag{6}$$

where g is the gravitational acceleration (9.8 m/s^2).

To assume that the flow density is a constant, the conservation equation is described as follows:

$$\rho\nabla\cdot\mathbf{u} = 0 \tag{7}$$

Furthermore, the constitutive equation related to the extra elastic stress is described as follows:

$$\lambda_{em}\overset{\nabla}{\mathbf{T}}_{em}+\mathbf{T}_{em} = 2\mu_{em}\mathbf{S} \tag{8}$$

$$\mathrm{S} = \frac{1}{2}(\nabla\mathrm{u}+(\nabla\mathrm{u})^{\mathrm{T}}) \tag{9}$$

where λ_{em} is the relaxation time (0.1 s), μ_{em} is the polymer viscosity (Pa·s), and $\mathbf{S}$ is the strain-rate tensor (Comsol Material Library). For oxyhydrogen flame polishing, μ_{em} mainly depends on the transient temperature T_w, which could be associated with the thermal power P in the simulation.

To accurately describe the viscoelasticity flow, the bonding mode of the microlens material units is set as Oldroyd-B. This phenomenon is expressed from kinetic theory as the suspension of a Hooke spring in a Newtonian solvent (Awan et al., 2022). Based on Eqs. (4–9), the viscoelasticity flow on the microlens surface could be simulated to analyse the nano-to-micro smoothing process.

3. Simulation and experiments

3.1. Microlens array smoothing simulation

As a thermal power P is set on the single microlens surface in Fig. 3a, the glass transition temperature T_m = 1215 °C is utilized to define the thermal transmission depth d_w. d_w increases sharply with increasing simulation time t_s at P = 10–400 W; it reaches a microlens height h_m of 30 μm at t_s = 0.09 ms or less. In addition, the temperature error of the whole microlens is less than 1% at t_s = 0.1 ms. This time is far less than the working time of each scanning with the velocity of 0.5–2 mm/s, which could be neglected. Thus the fluid viscosity η can be quantified by T_w to describe the viscoelasticity flow of the whole microlens regardless of the scanning velocity v_s. Further, the correlations between the η, P and T_w are given in Fig. 3b. T_w could be obtained by P based on the thermal transfer model, and then used to calculate η by the fitting function of Eq. (10) that described by Doremus (2002). T_w is positively correlated with P, and an increase in T_w may sharply decrease η. It enables to determine the condition parameters for the microlens smoothing simulation.

$$\eta = \begin{cases} 5.8\times10^{-8}\exp(515400/\mathrm{R}T_w) & T_w \geq 1400\ ^\circ\mathrm{C} \\ 3.8\times10^{-14}\exp(71200/\mathrm{R}T_w) & T_w < 1400\ ^\circ\mathrm{C} \end{cases} \tag{10}$$

where R is the molar gas constant, taken as 8.31 J/(mol·K).

In the simulation, a convex microstructure with a dip angle θ of 50°

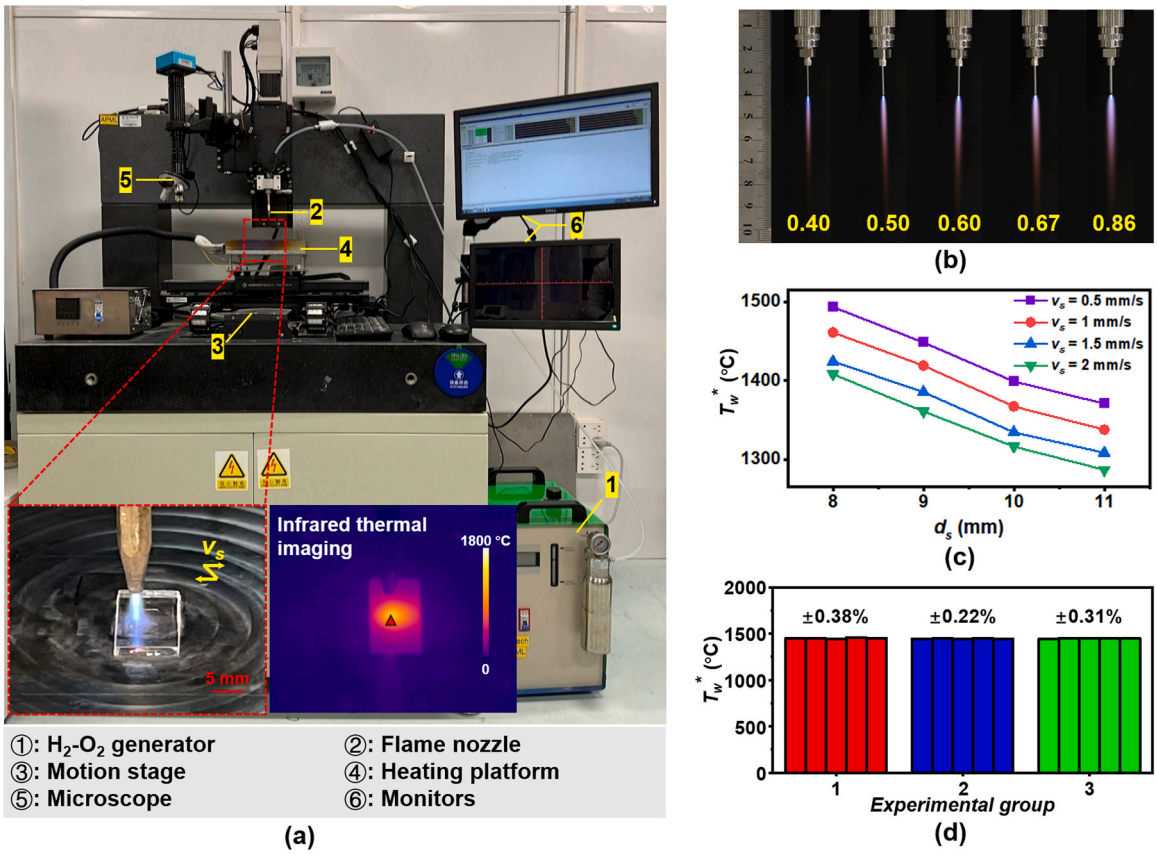

Fig. 4. Experimental setup and conditions for oxyhydrogen flame polishing. (a) Photograph of the experimental setup. (b) Flame nozzle with a diameter D of 0.4–0.86 mm. (c) Correlations between the measured transient temperature T_w^*, working distance d_s and scanning viscosity v_s. (d) Fluctuation of T_w^*.

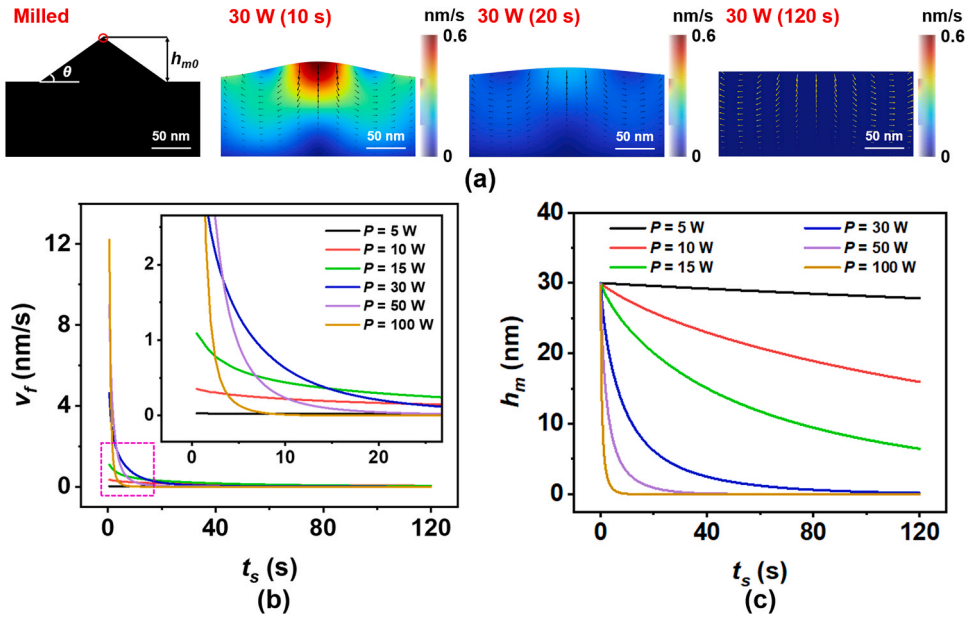

Fig. 5. Smoothing process simulation of the nanoscale convex microstructure. (a) Smoothing process with viscoelasticity flow. (b) Flow velocity v_f. (c) Microstructure height h_m versus simulation time t_s at a thermal power P of 5–100 W.

and an initial height h_{m0} of 30 μm is designed to analyze the smoothing process of rough nanoscale topography as well as the concave microstructure. The corresponding flow velocity v_f and microstructure height h_m are also investigated at a thermal power P of 5–100 W. In addition, the melting process of microscale residual steps is also analyzed by investigating the flow velocity v_f and the curvature radius r_s at P values of 10–400 W. The simulation time t_s is set to 120 s.

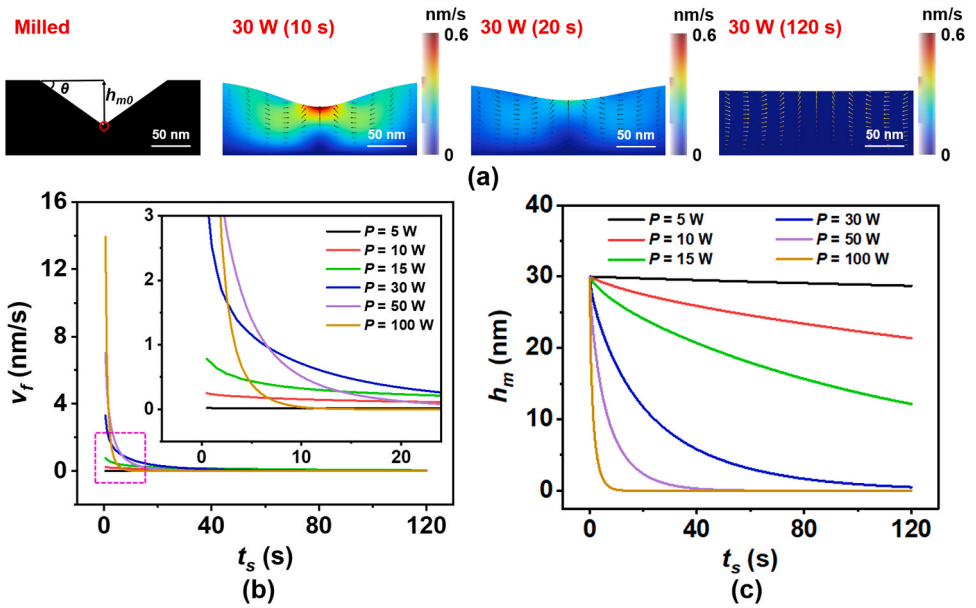

Fig. 6. Smoothing process simulation of the nanoscale concave microstructure. (a) Smoothing process with viscoelasticity flow. (b) Flow velocity v_f. (c) Microstructure height h_m versus simulation time t_s at a thermal power P of 5–100 W.

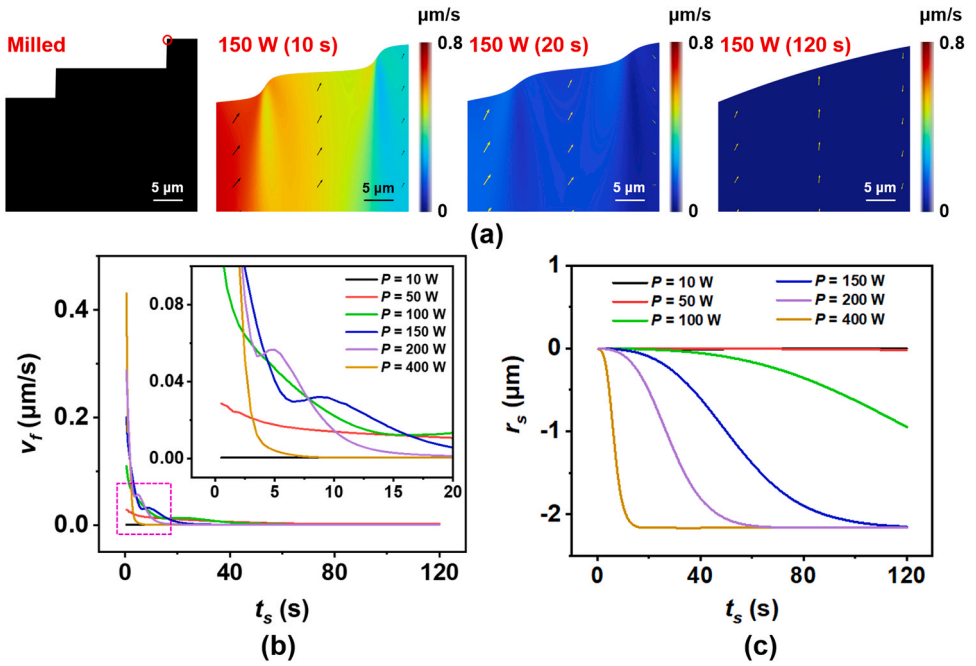

Fig. 7. Melting process simulation for microscale residual steps. (a) Melting process with viscoelasticity flow. (b) Flow velocity v_f. (c) Curvature radius r_s versus simulation time t_s at a thermal power P of 10–400 W.

3.2. Oxyhydrogen flame polishing experiment with the microlens

An on-machine experiment involving oxyhydrogen flame polishing is conducted to fabricate an ultrasmooth microlens array on silica glass using the experimental setup shown in Fig. 4a. An H_2-O_2 generator (1) is used to continuously trigger the oxyhydrogen flame during polishing. As the flame nozzle (2) is fixed on the gantry, a motion stage (3) with 1 μm resolution is used for microlens array scanning. To reduce the buckling deformation, a heating platform (4) is added to preheat the silica glass from room temperature to a maximum temperature of 600 °C. Furthermore, a 5×/10×/20× microscope (5) is used to collect on-site information about the workpiece zone, which is displayed on the monitors (6) for system localization.

To realize thermal uniformity on the microlens array surface, it is necessary to select a suitable flame nozzle before the experiment. As shown in Fig. 4b, the thermally affected diameter of the oxyhydrogen flame is approximately 2 times larger than the nozzle diameter D. Accordingly, a flame nozzle with $D = 0.6$ mm is selected by considering the designed microlens length of 1 mm and the suppressed buckling deformation in the small thermally affected zone. Furthermore, the influence of the working distance d_s and scanning viscosity v_s on transient temperature T_w should be determined for parameter selection. The scanning frequency is set to 8 times. As shown in Fig. 4c, the measured transient temperature T_w* decreases from 1600 °C to 1300 °C with

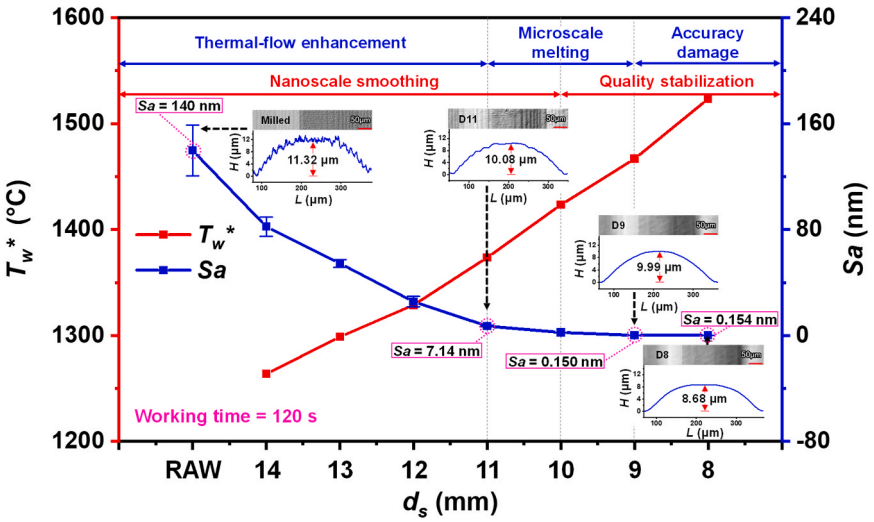

Fig. 8. Nano-to-micro viscoelasticity flow smoothing at working distance d_s in relation to the measured transient temperature T_w*.

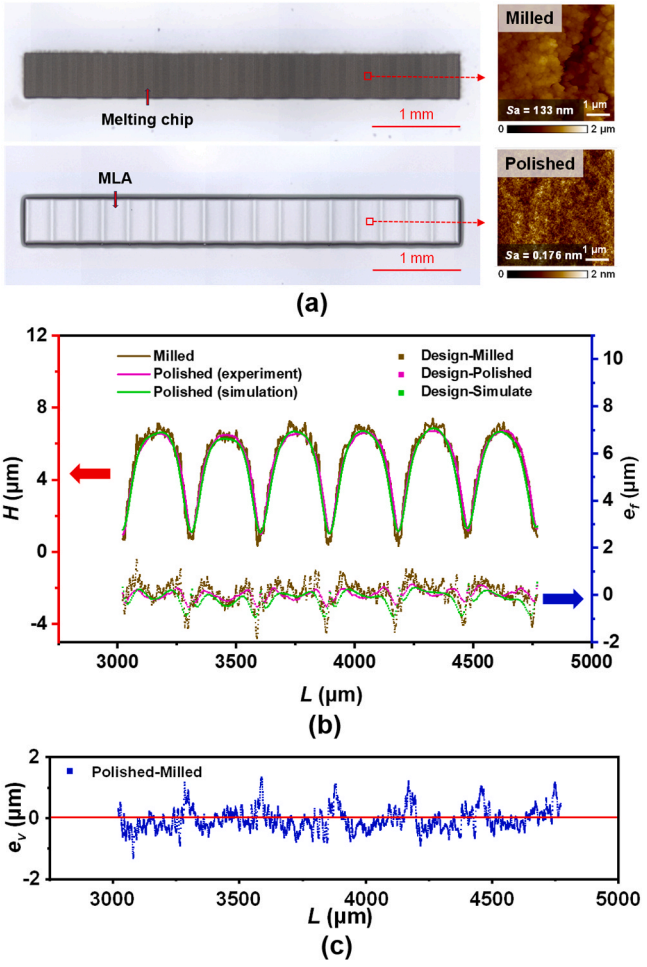

Fig. 9. Smoothing effect of oxyhydrogen flame polishing on a cylindrical microlens array. (a) Surface topography and its roughness *Sa*. (b) Surface topographical profile and form error e_f. (c) Profile variation e_v.

increasing d_s and v_s, and the temperature fluctuations in each group are less than 2%. Besides, temperature fluctuation of microlens surface during polishing needs to be investigated for stable smoothing effect. Three experimental groups are designed with the same conditions of d_s = 8 mm and v_s = 1 mm/s. As shown in Fig. 4d, the fluctuation of T_w* for each scanning at the first experimental group is not more than ±6 °C, about 0.38% of the mean value. The similar mean value and fluctuation of T_w* are also observed in the other two experimental groups, which can verify the repeatability and scalability of polishing process. This is the other reason why a constant fluid viscosity could be used at the specific thermal power for simulating material flow process.

In the experiment, first, single-point polishing at a working distance of d_s = 8–14 mm and a working time of t_w = 120 s is performed by associating the measured T_w* to analyse the nano-to-micro smoothing process. Second, an ultrasmooth cylindrical microlens array is fabricated at d_s = 8 mm and scanning velocity v_s = 1 mm/s, and scanning frequency of 72 times is used to evaluate the smoothing performance. Third, single-point polishing is applied to the spherical microlens at d_s = 9 mm and t_w = 120 s, and the corresponding surface quality is traced at intervals of 10 s. Furthermore, preheating temperature T_h = 300 °C and gas flux Q = 1 slm are set before polishing.

The transient temperature T_w is measured on-site by utilizing a FLIR A655sc infrared thermal camera (radiance: 0.86). The surface topography of the microlens (array) and its profile are evaluated via a KEYENCE VK-X1000 laser scanning confocal microscope (LSCM, magnification: 50×) and an ACCRETECH SNEX031DX-12 profilometer (scanning: 0.15 mm/s, tip angle: 60°, chamfer: 2 μm) to analyse the microlens height h_m and form error e_f. Furthermore, the atomic-level surface roughness *Sa* is measured by a BRUKER Dimension Edge atomic force microscope (AFM, zone: 5 μm×5 μm, working mode: tapping), followed by chemical element extraction utilizing a PHI 5000 Versaprobe III X-ray photoelectron spectrometer (XPS, radiation: AlKα, 1486.6 eV). The error bar of surface roughness is given by calculating a standard deviation of five experimental results measured from the same surface but different measurement zones. To evaluate the SSD before and after polishing, the microlens surface is postprocessed by HF etching (concentration: 14%).

4. Results and discussion

4.1. Smoothing of nanoscale roughness

Fig. 5 shows the smoothing process simulation of the nanoscale convex microstructure. The maximum flow velocity v_f at simulation time t_s = 0 increases with increasing thermal power P; this means that a large thermal energy may enhance the viscoelasticity flow on the microlens surface. As t_s increases from 0 to 120 s, the convex microstructure with a height h_{m0} = 50 μm is gradually smoothed into a plane, accompanied by

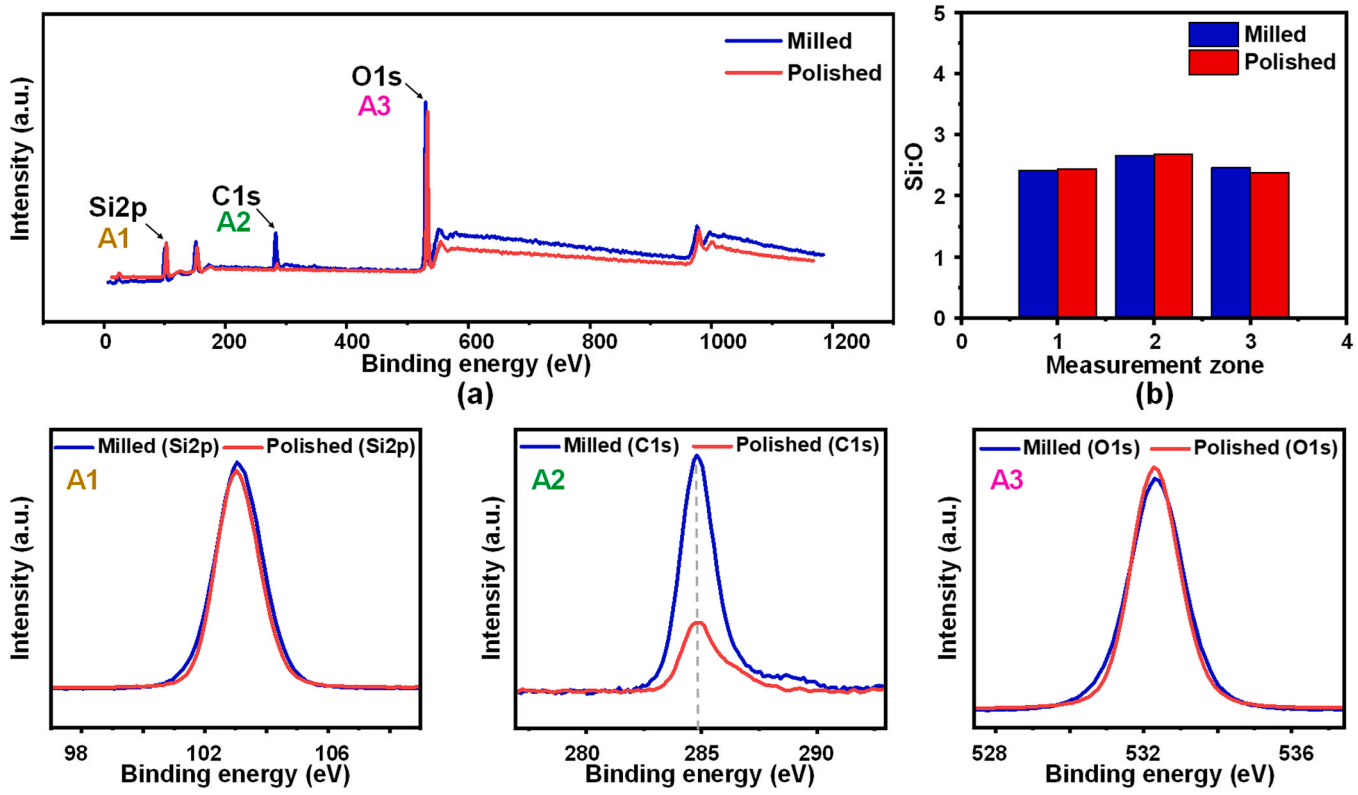

Fig. 10. XPS element detection for the milled and polished surfaces of cylindrical microlens. (a) Full spectrum. (b) ratios of Si and O elements (Si:O) at three measurement zones.

a decrease in v_f (see Fig. 5a). In this process, the viscoelasticity flow from the microstructure centre to both sides is triggered to slightly increase the base thickness to less than 7 nm. Although v_f decreases sharply at a large P of 30 W or more, enough thermal energy may decrease the microstructure height h_m to approach zero (see Figs. 5b and 5c).

Fig. 6 shows the smoothing process simulation of the nanoscale concave microstructure. The concave microstructure is also gradually smoothed to a plane, and the corresponding v_f decreases with increasing t_s from 0 to 120 s (see Fig. 6a). However, the viscoelasticity flow from both sides of the microstructure to the centre is triggered to slightly decrease the base thickness to less than 7 nm. Similarly, the microstructure height h_m may decrease, approaching zero at a large P of 30 W, even though v_f decreases sharply (see Figs. 6b and 6c). As a result, the nanoscale smoothing effect during oxyhydrogen flame polishing could be traced by precisely adjusting the viscoelasticity flow in reference to the transient temperature T_w, as shown in Fig. 3b.

4.2. Melting process of the microscale laser milling steps

Fig. 7 shows the melting process simulation of microscale residual steps. The maximum flow velocity v_f at simulation time $t_s = 0$ also increases with increasing thermal power P. As t_s increases from 0 to 120 s, the residual steps are gradually melted to smooth the microlens surface, accompanied by a decrease in v_f (see Fig. 7a). In this process, the viscoelasticity flow is dominated by the surface tension rather than by gravity, which contributes to the cylindrical formation of microlens profiles. At a large P of 150 W or more, the curvature radius r_s may decrease, approaching −2.16 mm even though v_f decreases sharply (see Figs. 7b and 7c). Thus, the microscale smoothing effect during oxyhydrogen flame polishing could also be traced by precisely adjusting the viscoelasticity flow in reference to the transient temperature T_w, as shown in Fig. 3b. In addition, the critical value of thermal power for microscale residual step melting is approximately four times greater than that for nanoscale microstructure smoothing; this means that the former should be considered the key factor for meeting the requirement of nano-to-micro viscoelasticity flow smoothing.

In this simulation, the curvature radius r_s converges to a certain constant value due to the set substrate boundaries. Actually, the r_s would finally increase to an infinite value as the microlens shape is damaged to be a plane, but this model still enables to describe the step melting process in the term of conformal polishing.

4.3. Transient temperature for nano-to-micro viscoelasticity flow smoothing

Fig. 8 shows the nano-to-micro viscoelasticity flow smoothing at working distance d_s in relation to the measured transient temperature T_w*. As the d_s decreases from 14 mm to 8 mm during single-point polishing, the T_w* increases from 1260 °C to 1520 °C, which contributes to a decrease in the surface roughness Sa from 140 nm to 0.15 nm. The corresponding error bar also decreased due to the stable polishing process. When the T_w* reaches 1420 °C or more, an increase in the atomic level Sa might be achieved, during which the material tends to be stable. Thus, a critical value of 1420 °C could be defined to distinguish the nanoscale smoothing stage from the quality stabilization stage. In addition, the T_w* of 1470 °C might totally melt the residual steps compared to the T_w* of 1365 °C with no step melting. This phenomenon is similar to the results of the simulation. Additionally, for T_w* values greater than 1470 °C, the microlens height h_m decreased to less than 10 μm, which decreased the shape accuracy. Accordingly, the thermal-flow enhancement stage, microscale melting stage and accuracy damage stage are divided into two critical values of 1365 °C and 1470 °C.

As a result, nano-to-micro viscoelasticity flow smoothing may be achieved by precisely triggering the critical transient temperature during oxyhydrogen flame polishing. It is also known that the critical transient temperatures of the nanoscale smoothing-to-stabilization stage

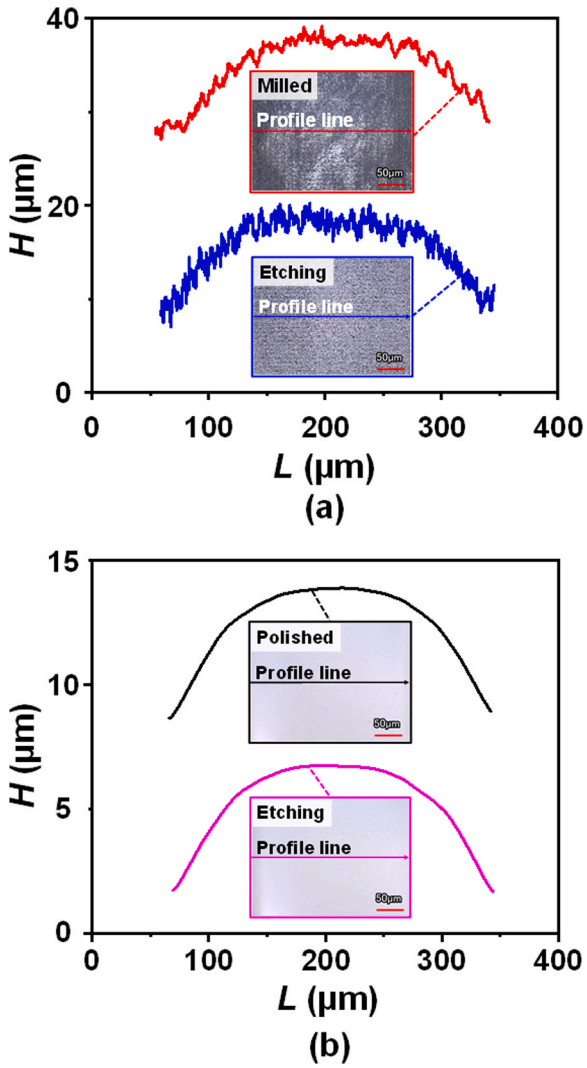

Fig. 11. Etched surface topographical profile. (a) Milled cylindrical microlens. (b) Polished cylindrical microlens.

and microscale melting-to-damage stage change at different working times t_w based on microlens smoothing simulations. For actual application, the process variables should be carefully selected to guarantee the smoothing effect.

4.4. Oxyhydrogen flame polishing of a cylindrical microlens array

With a working time of $t_w = 120$ s for single microlens smoothing, suitable process variables, namely, working distance $d_s = 8$ mm and scanning velocity $v_s = 1$ mm/s, are utilized in oxyhydrogen flame polishing of a cylindrical microlens array to trigger a critical transient temperature of 1470 °C. The corresponding surface topographical profiles of the microlens array are shown in Fig. 9. The milled microlens array is efficiently smoothed to transparency after polishing, and the surface roughness *Sa* of 133±10 nm sharply decreases to 0.176 ±0.01 nm (see Fig. 9a). Due to the melted residual steps and the smoothed rough topography, the form error e_f of ±1.7 μm decreases to ±0.5 μm or less, up to 70%, which contributes to the improvement in microlens array uniformity. This smoothing effect may meet the beam shaping requirements. In addition, the simulated microlens profile and its e_f after polishing (green) in Fig. 9b fit well with the experimental profiles (pink). Accordingly, the simulative model may predict the polished profile for process variable optimization. It is also seen in Fig. 9c that profile variation e_v below the red line is observed in the centre of each microlens, and the e_v above the red line is observed on the both sides of each microlens. This means the molten material at the top of microlens tends to flow down to the bottom with no material removal in the polishing process, which is also identical to the simulative results.

It has been reported that hydroxyl groups may induce nanopore formation in silica to consequently reduce its mechanical strength (Fett et al., 2018), and affect the optical transmittance of silica glass in the mid-infrared spectral region (Velmuzhov et al., 2018). Therefore, avoiding the introduction of hydroxyl groups on the microlens surface is an important step for industrial applications. Fig. 10a shows the full spectrum of the milled and polished surfaces of cylindrical microlens obtained by XPS. Considering the influence on X-ray photoelectron intensity, the position of the C1s peak is chosen to align the abscissas of the two measured curves. By comparing the position of other elements, it is proven that the bonding form of polished surface does not change. Then, the Si2p photoelectron intensity of the milled surface is adjusted to match that of the polished one. Accordingly, the corresponding ratios of Si and O elements (Si:O) could be calculated by the Si2p and O1s peaks in A1 and A3 to judge whether the hydroxyl groups are introduced or not. The C1s peaks of the milled and polished surfaces in A2 change significantly, which is attributed to contamination of C elements in the instrument. Fig. 10b shows the Si:O of the milled and polished surfaces at three measurement zones. Compared to the milled surface, the changes in Si:O of polished one are 1.2%, 0.8%, and −3.6%, respectively. This means the oxyhydrogen flame polishing does not introduce hydroxyl groups on the microlens surface.

Furthermore, the etched surface topographical profiles of the milled and polished cylindrical microlenses are given in Fig. 11. The surface topography of the milled microlens is rough, and an SSD is also observed after HF etching (see Fig. 11a). In contrast, the polished microlens surface with a smooth topographical profile present less SSD after HF etching (see Fig. 11b); this means that the viscoelasticity flow in oxyhydrogen flame polishing may require a nanoscale SSD for ultra-smooth microlens fabrication.

Shen et al. (2005) assert that SSD is likely to decrease the laser-induced damage threshold (LIDT), a critical factor in the utilization of optical components within lasers. The LIDT represents the maximum laser power a component can withstand without harm, with higher values being preferable for extending the component lifespan. Consequently, maintaining low SSD becomes highly important in high-energy laser applications to ensure optimal performance and longevity of optical components in the face of intense laser conditions.

4.5. Application of oxyhydrogen flame polishing on a spherical microlens

Based on the abovementioned analysis, single-point polishing with an oxyhydrogen flame is also applied to a spherical microlens by considering the critical transient temperature of 1470 °C, and the corresponding smoothing effect is shown in Fig. 12. The milled microlens with residual steps and rough topography produces a large surface roughness *Sa* of 125 nm (see Fig. 12a). As the working time t_w increases from 0 to 120 s during polishing, the microlens is smoothed to sharply decrease the *Sa* to the atomic level, after which the *Sa* finally stabilizes at 0.13 nm (see Fig. 12c). Herein, the rough topography is slightly smoothed, but no residual step melts at $t_w = 40$ s (see Fig. 12b); this is because nanoscale topographic smoothing is triggered prior to microscale step melting in reference to the transient temperature (see Fig. 8).

Additionally, the *Sa* and its error bar decrease with increasing t_w (see Fig. 12d). The polishing does not damage the microlens height, decreasing the form error e_f from ±1.42 μm to ±0.54 μm (see Fig. 12e). In the Fig. 12f, profile variation e_v below the red line is also observed in the central of spherical microlens, while the e_v above the red line is hardly observed on its two sides. The material flow thickness in the centre of spherical microlens is about 2 μm. Considering that only one microlens is fabricated on the glass substrate, the molten material flows outward along the surface and results in a small profile variation at the

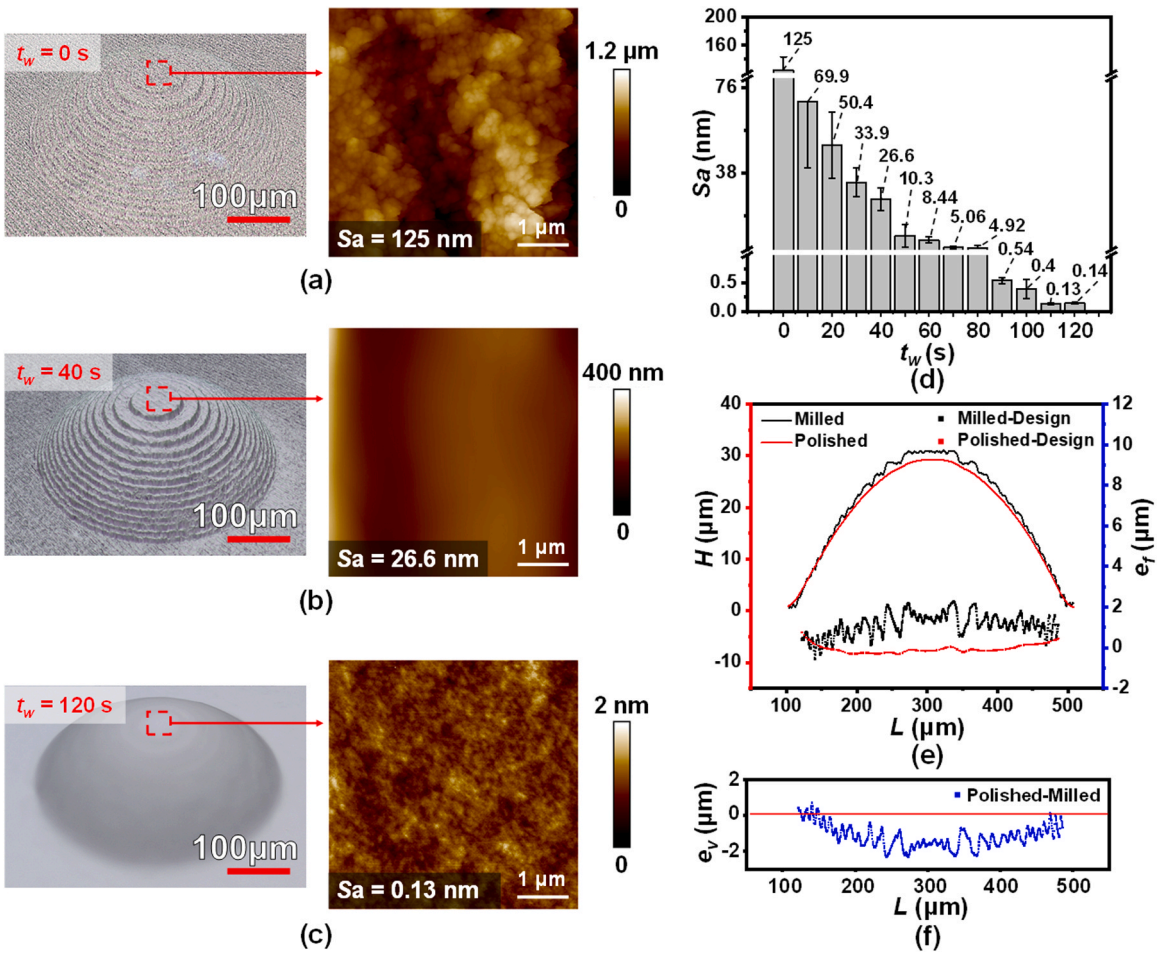

Fig. 12. Smoothing effect of oxyhydrogen flame polishing on a spherical microlens. (a-c) Surface topography and its roughness *Sa* at working times t_w = 0, 40 s, 120 s. (d) Correlation between *Sa* and t_w. (e) Topographical profile and form error e_f. (f) Profile variation e_v.

bottom of microlens. As a result, oxyhydrogen flame polishing of various microlenses on silica glass may be achieved by conforming to nano-to-micro viscoelasticity flow smoothing at suitable transient temperatures.

Kahle et al. (2022) proposed a CO_2 laser polishing method for microlens arrays, aiming to streamline polishing processes after laser milling. However, CO_2 laser polishing resulted in material ablation, removing a 6 μm layer from the top of the microlens. In comparison, the oxyhydrogen flame polishing results in no material removal, and the material can only undergo flow at a scale as fine as 1 μm without altering the contour accuracy. This observation highlights that, compared to a CO_2 laser, an oxyhydrogen flame is more effective at polishing microlens arrays.

5. Conclusions

In this study, the oxyhydrogen flame polishing is employed after laser milling to efficiently fabricate ultrasmooth surface of microlens array on silica glass substrate, revealing its viscoelasticity flow at nano/microscale. The corresponding simulation and experiment are carried out to obtain the following conclusions:

(1) In the simulative polishing process, large thermal power derived from the oxyhydrogen flame may induce nano-to-micro viscoelasticity flow at a high velocity to smooth the microlens under surface tension and gravity. While nanoscale topography smoothing is triggered prior to microscale step melting.
(2) Increasing the transient temperature decreases the microlens surface roughness to the atomic level. For a working time of 120 s, the critical values of 1420 °C and 1470 °C are determined to indicate the nanoscale smoothing-to-stabilization stage and the microscale melting-to-damage stage, respectively.
(3) Micro/nanoscale viscoelasticity flow smoothing efficiently achieves the hydroxyl-free surface of cylindrical microlens array with 0.176-nm-*Sa*, ±0.5-μm-e_f and a decreased SSD. This approach also improves the surface quality of the spherical microlenses at suitable transient temperatures.

Generally, the precision/ultraprecision manufacturing of cylindrical or spherical microlens arrays mainly depends on femtosecond laser milling, which has low efficiency and surface quality. However, oxyhydrogen flame polishing is likely to change the shape accuracy of microlenses at large transient temperatures and working times. This phenomenon may be utilized to tune the prismatic microlens to the required cylindrical or spherical microlens. Hence, the corresponding control mechanism will be further studied in the future for high-efficiency and high-quality microlens manufacturing.

CRediT authorship contribution statement

Yi Zhang: Validation, Supervision, Software, Project administration, Methodology, Formal analysis. **Xingzhan Li:** Supervision, Software, Methodology, Formal analysis, Conceptualization. **Qian Wang:** Supervision, Software, Methodology, Formal analysis, Data curation. **Peng Zhou:** Software, Methodology, Investigation, Formal analysis, Conceptualization. **Jin Tang:** Writing – original draft, Validation, Software, Methodology, Investigation, Formal analysis, Data curation. **Linfeng**

Zhang: Software, Methodology, Formal analysis, Data curation. **Quanpeng He:** Writing – review & editing, Supervision, Methodology, Conceptualization. **Hui Deng:** Writing – review & editing, Supervision, Funding acquisition, Conceptualization.

Declaration of Competing Interest

The authors declare the following financial interests/personal relationships which may be considered as potential competing interests: Hui Deng reports financial support was provided by National Natural Science Foundation of China

Acknowledgements

This work is supported by the National Key Research and Development Program of China (2023YFE0202900), the National Natural Science Foundation of China (52375437, 52035009), and the Natural Science Foundation of Guangdong Province (2023A1515011461). The authors acknowledge the assistance of SUSTech Core Research Facilities. The present study was also supported by Shenzhen Engineering Research Center for Semiconductor-specific Equipment.

References

Awan, A.U., Riaz, S., Abro, K.A., Siddiqa, A., Ali, Q., 2022. The role of relaxation and retardation phenomenon of Oldroyd-B fluid flow through Stehfest's and Tzou's algorithms. Nonlinear Eng. 11, 35–46. https://doi.org/10.1515/nleng-2022-0006.

Bardinal, V., Daran, E., Leichle, T., Vergnenegre, C., Levallois, C., Camps, T., Conedera, V., Doucet, J.B., Carcenac, F., Ottevaere, H., Thienpont, H., 2007. Fabrication and characterization of microlens arrays using a cantilever-based spotter. Opt. Express 15, 6900–6907. https://doi.org/10.1364/oe.15.006900.

Boyd, K., Ebendorff-Heidepriem, H., Monro, T.M., Munch, J., 2012. Surface tension and viscosity measurement of optical glasses using a scanning CO_2 laser. Opt. Mater. Express 2, 1101–1110. https://doi.org/10.1364/OME.2.001101.

Brar, R.S., Surman, P., Sexton, I., Hopf, K., 2010. Multi-user glasses free 3D display using an optical array. IEEE, pp. 1–4. https://doi.org/10.1109/3DTV.2010.5506487.

Changming, X., Guiyao, Z., Ying, H., Xingtao, Z., Chao, W., Lantian, H., 2013. Investigation on preparation and spectroscopic properties of Yb^{2+}-doped silica-based glass prepared by the oxyhydrogen flame fusing process. Opt. Mater. 35, 2561–2564. https://doi.org/10.1016/j.optmat.2013.07.025.

Cheng, S., 2021. Viscosity-temperature relation based on the evolution of medium-range structures of silica. J. Non-Cryst. Solids 557, 120582–120588. https://doi.org/10.1016/j.jnoncrysol.2020.120582.

Comsol Material Library. ⟨https://www.comsol.com/material-library⟩.

Corning Fused SilicaTechnical Data Sheet. ⟨https://www.corning.com/media/worldwide/csm/documents/HPFS_Product_Brochure_All_Grades_2015_07_21.pdf⟩.

Doremus, R.H., 2002. Viscosity of silica. J. Appl. Phys. 92, 7619–7629. https://doi.org/10.1063/1.1515132.

Du, H., Jiang, M., Zhu, Z., Wang, Z., To, S., 2022. Ultraprecision tool-servo cutting of pure nickel for fabricating micro/nanostructure arrays. Mater. Des. 221, 110913–110924. https://doi.org/10.1016/j.matdes.2022.110913.

Du, X., Florian, C., Arnold, C.B., 2023. Single-lens dynamic z-scanning for simultaneous in situ position detection and laser processing focus control. Light Sci. Appl. 12, 274. https://doi.org/10.1038/s41377-023-01303-2.

Feng, C., Hewei, L., Qing, Y., Xianhua, W., Cong, H., Hao, B., Weiwei, L., Jinhai, S., Xun, H., 2010. Maskless fabrication of concave microlens arrays on silica glasses by a femtosecond-laser-enhanced local wet etching method. Opt. Express 18, 20334–20343. https://doi.org/10.1364/OE.18.020334.

Fett, T., Schell, K.G., Hoffmann, M.J., Wiederhorn, S.M., 2018. Effect of damage by hydroxyl generation on strength of silica fibers. J. Am. Ceram. Soc. 101, 2724–2726. https://doi.org/10.1111/jace.15508.

He, T., Wei, C., Jiang, Z., Zhao, Y., Shao, J., 2018. Super-smooth surface demonstration and the physical mechanism of CO(2) laser polishing of fused silica. Opt. Lett. 43, 5777–5780. https://doi.org/10.1364/OL.43.005777.

Hildebrand, J., Hecht, K., Bliedtner, J., Müller, H., 2011. Laser Beam Polishing of Quartz Glass Surfaces. Phys. Procedia 12, 452–461. https://doi.org/10.1016/j.phpro.2011.03.056.

Huang, S., Li, M., Shen, L., Qiu, J., Zhou, Y., 2018. Fabrication of high quality aspheric microlens array by dose-modulated lithography and surface thermal reflow. Opt. Laser Technol. 100, 298–303. https://doi.org/10.1016/j.optlastec.2017.10.026.

Kahle, M., Conrad, D., Fricke, S., Wilkens, L., Haberl, A., Fütterer, G., Fähnle, O.W., Wünsche, C., 2022. Direct manufacturing of microlens arrays via laser ablation and polishing. Proc. SPIE 12298, 1–5. https://doi.org/10.1117/12.2631713.

Kostyuk, G.K., Zakoldaev, R.A., Sergeev, M.M., Yakovlev, E.B., 2016. Microlens array fabrication on fused silica influenced by NIR laser. Appl. Phys. B 122, 1–8. https://doi.org/10.1007/s00340-016-6379-y.

Liang, Y., Zhu, T., Du, X., Xu, J., Fan, S., Wang, H., 2022. Fabrication of a microlens array on diamond for Shack-Hartmann sensor. Diam. Relat. Mater. 121, 108783–108788. https://doi.org/10.1016/j.diamond.2021.108783.

Ma, Y., Yi, Y., Li, X., Su, C., Zhang, M., Geng, T., Sun, W., Yuan, L., 2021. Refractometer based on fiber Mach-Zehnder interferometer composed of two micro bending cores. Opt. Express 29, 31443–31454. https://doi.org/10.1364/OE.435442.

Mahrenholtz, H., 2008. Fire Polishing with Premixing Technology. J. Am. Ceram. Soc. 25, 141–152. https://doi.org/10.1002/9780470294857.ch10.

Marimuthu, S., Triantaphyllou, A., Antar, M., Wimpenny, D., Morton, H., Beard, M., 2015. Laser polishing of selective laser melted components. Int. J. Mach. Tool. Man. 95, 97–104. https://doi.org/10.1016/j.ijmachtools.2015.05.002.

Matthews, M.J., Yang, S.T., Shen, N., Elhadj, S., Raman, R.N., Guss, G., Bass, I.L., Nostrand, M.C., Wegner, P.J., 2015. Micro-Shaping, Polishing, and Damage Repair of Fused Silica Surfaces Using Focused Infrared Laser Beams. Adv. Eng. Mater. 17, 247–252. https://doi.org/10.1002/adem.201400349.

Microlens Array Specifications by Coherent Corp. ⟨https://www.coherent.com/optics/general-optics/lenses-mirrors/micro-lens-arrays⟩.

Pfefferkorn, F.E., Duffie, N.A., Li, X., Vadali, M., Ma, C., 2013. Improving surface finish in pulsed laser micro polishing using thermocapillary flow. CIRP Ann. -Manuf. Techn. 62, 203–206. https://doi.org/10.1016/j.cirp.2013.03.112.

Qiao, L., He, F., Wang, C., Cheng, Y., Sugioka, K., Midorikawa, K., 2010. A microfluidic chip integrated with a microoptical lens fabricated by femtosecond laser micromachining. Appl. Phys. A 102, 179–183. https://doi.org/10.1007/s00339-010-6096-z.

Ross, C.A., MacLachlan, D.G., Smith, B.J.E., Beck, R.J., Shephard, J.D., Weston, N., Thomson, R.R., 2020. A Miniature Fibre-Optic Raman Probe Fabricated by Ultrafast Laser-Assisted Etching. Micro - Basel 11, 185. https://doi.org/10.3390/mi11020185.

Savander, P., 1994. Microlens Arrays Etched into Glass and Silicon. Opt. Laser Eng. 20, 97–107. https://doi.org/10.1016/0143-8166(94)90020-5.

Shen, J., Liu, S., Yi, K., He, H., Shao, J., Fan, Z., 2005. Subsurface damage in optical substrates. Optik 116, 288–294. https://doi.org/10.1016/j.ijleo.2005.02.002.

Sohn, I., Choi, H., Noh, Y., Kim, J., Ahsan, M.S., 2019. Laser assisted fabrication of microlens array and characterization of their beam shaping property. Appl. Surf. Sci. 479, 375–385. https://doi.org/10.1016/j.apsusc.2019.02.083.

Velmuzhov, A.P., Sukhanov, M.V., Churbanov, M.F., Kotereva, T.V., Shabarova, L.V., Kirillov, Y.P., 2018. Behavior of Hydroxyl Groups in Quartz Glass during Heat Treatment in the Range 750–950°C. Inorg. Mater. + 54, 925–930. https://doi.org/10.1134/S0020168518090169.

Wang, C., Zhang, Z., Cheung, C.F., Luo, W., Loh, Y.M., Lu, Y., Kong, L., Wang, S., 2022. Maskless fluid jet polishing of optical structured surfaces. Precis Eng. 73, 270–283. https://doi.org/10.1016/j.precisioneng.2021.09.010.

Wang, T.T., Zupko, H.M., 2006. Strengths and diameter variations of fused silica fibers prepared in oxy-hydrogen flames. Fiber Integr. Opt. 3, 73–87. https://doi.org/10.1080/01468038008202116.

Wang, Z., Zhu, G., Huang, Y., Zhu, X., Zhu, C., 2015. Analytical model of microlens array system homogenizer. Opt. Laser Technol. 75, 214–220. https://doi.org/10.1016/j.optlastec.2015.07.001.

Weingarten, C., Schmickler, A., Willenborg, E., Wissenbach, K., Poprawe, R., 2017. Laser polishing and laser shape correction of optical glass. J. Laser Appl. 29, 011702 https://doi.org/10.2351/1.4974905.

Yao, W., Zheng, L., Zhang, H., 2015. Modeling analysis on the silica glass synthesis in a hydrogen diffusion flame. Int. J. Heat Mass Trans. 81, 797–803. https://doi.org/10.1016/j.ijheatmasstransfer.2014.11.004.

Yuan, C., Kowsari, K., Panjwani, S., Chen, Z., Wang, D., Zhang, B., Ng, C.J., Alvarado, P.V.Y., Ge, Q., 2019. Ultrafast Three-Dimensional Printing of Optically Smooth Microlens Arrays by Oscillation-Assisted Digital Light Processing. ACS Appl. Mater. Interfaces 11, 40662–40668. https://doi.org/10.1021/acsami.9b14692.

Zhang, L., Yan, J., 2022. Amorphous Carbon Coated Silicon Wafer as Mold Insert for Precision Glass Molding. Procedia CIRP 108, 525–530. https://doi.org/10.1016/j.procir.2022.03.082.

Zhang, L., Yi, A.Y., Yan, J., 2022. Flexible fabrication of Fresnel micro-lens array by off-spindle-axis diamond turning and precision glass molding. Precis Eng. 74, 186–194. https://doi.org/10.1016/j.precisioneng.2021.11.013.

Zhang, Y., Tang, J., Liang, S., Zhao, J., Hua, M., Zhang, C., Deng, H., 2024. Atomic-scale smoothing of semiconducting oxides via plasma-enabled atomic-scale reconstruction. Int. J. Mach. Tools Manuf. 196, 104119 https://doi.org/10.1016/j.ijmachtools.2024.104119.

Zhao, Q., Li, H., Lv, J., Liu, X., Zhang, F., Jiang, S., Ma, L., Wang, C., Ni, J., Peng, G., 2020. Adhesive-free bonding fiber optic Fabry–Perot pressure sensor based on oxy-hydrogen flame welding and spiral tube. Opt. Commun. 476, 126307 https://doi.org/10.1016/j.optcom.2020.126307.